Structural behavior of GFRP-concrete composite beams

Mohammed Abdel-Rahman M. Khalil
Faculty of Engineering, Helwan University, Egypt.
mamkhalil@m-eng.helwan.edu.eg

Ata El-Kariem Shoeib Soliman, Alaa Gamal Sheriff, Mohammed M. Salem
Faculty of Engineering, Mataria, Helwan University, Egypt.
atta_alsayed@m-eng.helwan.edu.eg, agbsherif@gmail.com, Mohamedsalem@m-eng.helwan.edu.eg

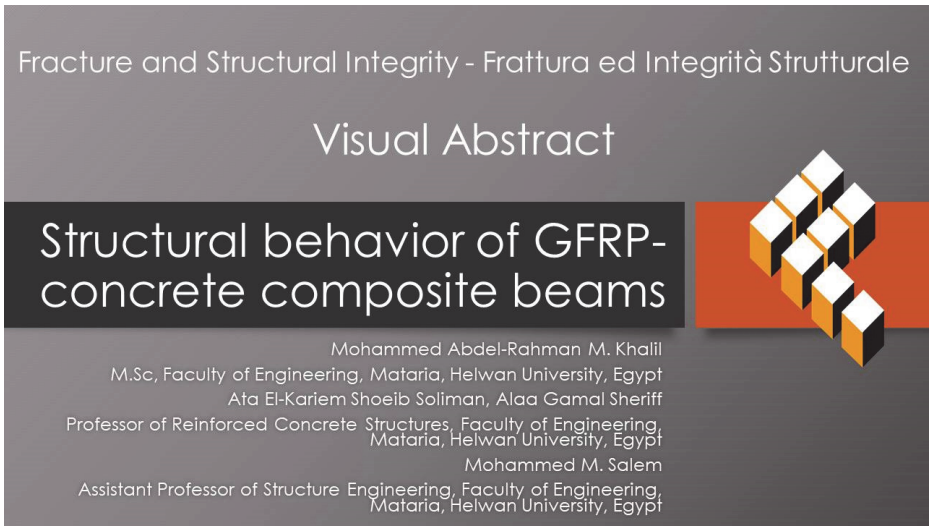

Citation: Khalil, M., Soliman, A., Sheriff, A., Salem, M., Structural Behavior Of GFRP-Concrete Composite Beams, Fracture and Structural Integrity, 72 (2025) 193-210.

Received: 19.01.2025
Accepted: 08.03.2025
Published: 11.03.2025
Issue: 04.2025

KEYWORDS. GFRP I-Section, Composite beams, Reinforced concrete, Analysis, Experimental and theoretical study, Fire.

INTRODUCTION

In recent times, Glass Fiber Reinforced Polymer (GFRP) has become an alternative to steel as structural materials, due to its high strength, light weight, low cost , being a corrosion-resistant material, easier to installed reducing the overall structure weight. The GFRP sections are non-metallic, so they are not susceptible to electrochemical corrosion that can occur when exposed to chloride in coastal environments. GFRP have been widely used in civil engineering applications. This study deals with optimizing the design of GFRP-reinforced composite concrete beams leading to greater savings. There are many previous studies that have been conducted on the behavior of composite beams reinforced with GFRP I-section and steel bars [1 to 19]. Ibrahim T. [1] investigated in this study the flexural performance of RC specimens composite with encased pultruded GFRP I-sections and effect of using shear studs shear studs to improve the composite interaction between the GFRP beam and concrete. Zhang P. [2] studied of GFRP I-shaped profile beams strengthened with a layer of high strength concrete slab on top and carbon FRP (CFRP) sheets on the web under bending loading, and all members showed positive effect for the ultimate bearing capacity and initial rigidity. Another study by Ali M. [3] investigated the flexural behavior of pultruded GFRP I–section strengthened by shear webs with GFRP T–section stiffeners in conjunction with concrete slabs, as the results indicated that the flexural and shear strength were improved. Enas M. [4] confirmed that the reduction in the capacity was about 25% for the encased GFRP beams with exposure to fire under 700°C for one hour.

Shahaji P. [15] conducted an experimental study on composite beam reinforced with pultruded GFRP I-profile & C-channel profile in the center and bottom side to determine the load capacity of the beams under four-point bending. The results showed that the beam with GFRP I-section carries more load compared to the beam with GFRP C-channel profile. The beam with GFRP I-section at the bottom carries more loads compared to the beam with GFRP I-section at the center. Research studies [20, 21, 22] have shown that fire can significantly affect the strength and stiffness of GFRP-concrete composite beams, leading to structural failure. Aydin F. [22] conducted an experimental investigation to determine the compressive and tensile strengths of the GFRP section at 13 various temperatures. According to the test results, the compressive and tensile strengths for GFRP composite beams were 75% and 28% respectively lower than conventional reinforced beams at 100°C. The GFRP profiles lost all of its compressive strength and about 50% of its tensile strength at temperature 200°C. Generally, GFRP sections have sensitivity at high temperatures and relative durability at low temperature.

The technical previous studies did not make a focus on the behaviour of the tension side of beams, internally or externally reinforced by GFRP I–section, leading to the preparation of this Research Paper. According to the experimental and analytical results of this study, a practical guideline for the use of GFRP-concrete composite beams that leads to the most economical design has been proposed.

EXPERIMENTAL PROGRAM

The experimental study of this research considers the behavior of composite reinforced GFRP concrete beams under four-points bending. The details of specimens are presented in (Fig.1), where:

1. RC: Conventional reinforced concrete specimen.
2. RCxGI-I: Composite Reinforced concrete specimens with GFRP I-Section Internally at the bottom. x: the testing group number.
3. RCxGI-E: Composite Reinforced concrete specimens with GFRP I-Section Externally at the bottom with shear connectors.
4. RCxGI-F: Composite Reinforced concrete specimens with GFRP I-Section Internally at the bottom with exposing to fire under 500°C for 90 minutes.

Test Parameters and specimen details

For three different beam depths (300 mm, 400 mm and 500 mm), three main parameters were considered. The parameters are GFRP I-sections positioned internally; externally; and internally with fire exposure to 500°C for 90 minutes. Each parameter was studied three times according to the variable beam depths, as all of these parameters were studied with variable depths. The dimensions of specimens and the details of reinforcement of the tested beams are shown in Tab. 1 and Fig. 1**.** Twelve tested specimens were prepared and tested in this experimental study with 2040 mm total length and 200 mm width. All tested beam specimens were 2R12 mm in bottom and 2R10 mm in top and 8 mm at 100 mm stirrups**.** The dimensions of GFRP I-section are 100 mm × 80 mm × 5.5 mm. The specimens were divided into four groups shown in Tab. 1. The first group has three control (Reference) tested beam specimens; the second group has three tested specimens internally reinforced with GFRP I-section, the third group has three beam specimens externally reinforced with GFRP I-section and the fourth group has three tested specimens internally reinforced with GFRP I-section with fire exposure under 500°C for 90 minutes.

Group	Specimens code	Dim. (mm)			Steel			Fire	GFRP I -sec
		L	b	t	Bot.	Top	Stirrups		
G1	RC1	2040	200	300	2R12	2R10	R8@100 mm	----	----
	RC2	2040	200	400	2R12	2R10	R8@100 mm	----	----
	RC3	2040	200	500	2R12	2R10	R8@100 mm	----	----
G2	RC1GI-I	2040	200	300	2R12	2R10	R8@100 mm	----	Int.
	RC2GI-I	2040	200	400	2R12	2R10	R8@100 mm	----	Int.
	RC3GI-I	2040	200	500	2R12	2R10	R8@100 mm	----	Int.
G3	RC1GI-E	2040	200	300	2R12	2R10	R8@100 mm	----	Ext.
	RC2GI-E	2040	200	400	2R12	2R10	R8@100 mm	----	Ext.
	RC3GI-E	2040	200	500	2R12	2R10	R8@100 mm	----	Ext.
G4	RC1GI-I-F	2040	200	300	2R12	2R10	R8@100 mm	Fire	Int.
	RC2GI-I-F	2040	200	400	2R12	2R10	R8@100 mm	Fire	Int.
	RC3GI-I-F	2040	200	500	2R12	2R10	R8@100 mm	Fire	Int.

Table 1: Designations of tested beams.

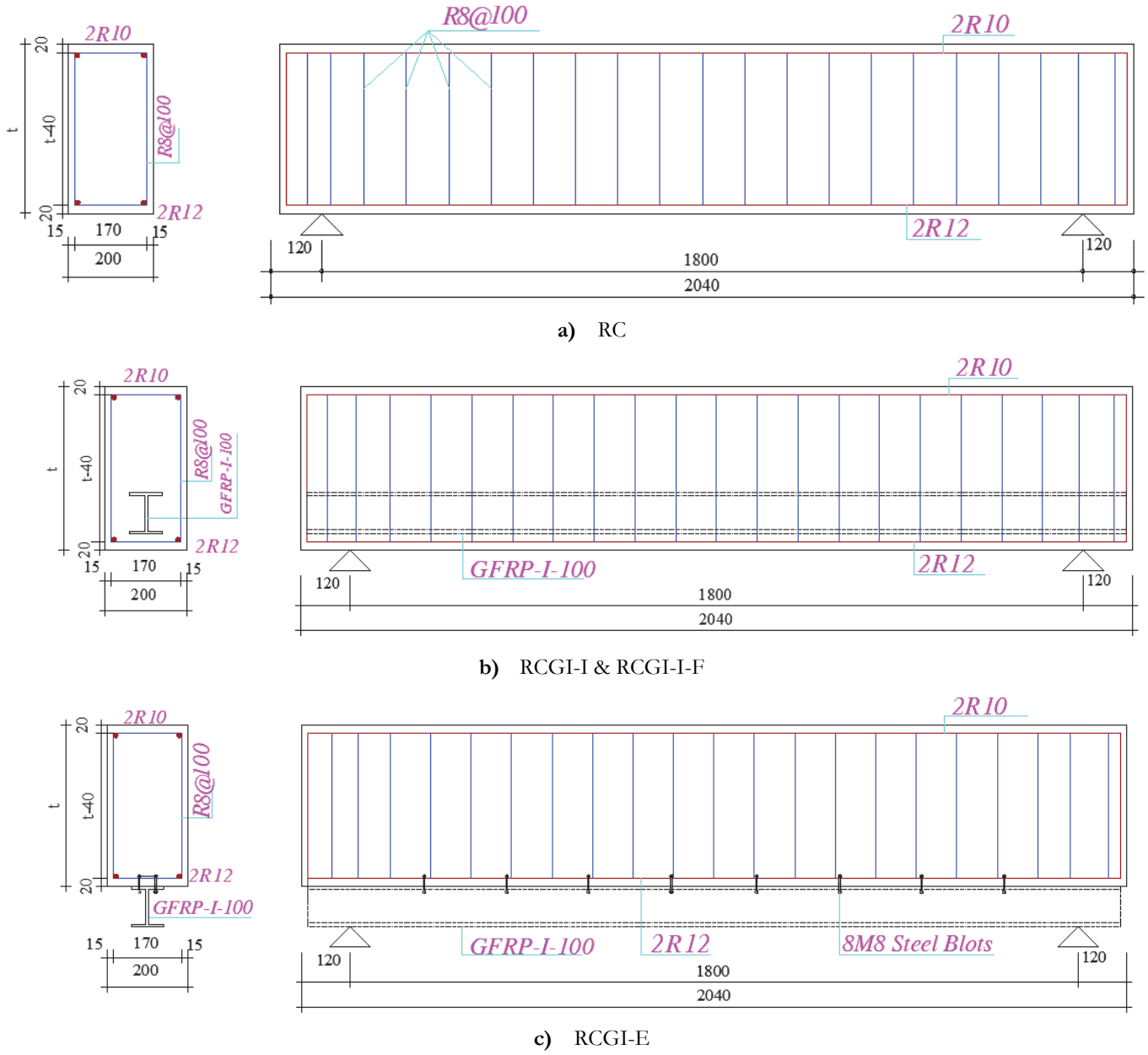

a) RC

b) RCGI-I & RCGI-I-F

c) RCGI-E

Figure 1: Specimen details of the tested beams.

The RC tested specimens have external GFRP I-sections attached to the bottom of the specimens by eight U- shape shear connectors, as shown in Fig. 2a, with diameter 8 mm, height 140 mm and spacing 200 mm.
The GFRP I-section support regions were encased in 240 mm length with beam wide reinforced concrete blocks to prevent a premature local crushing failure.
The blocks, as shown in Fig. 2b, have two longitudinal steel bars with 10 mm diameters and five U-shaped stirrups with 10 mm diameter.

Material properties

The concrete mix was designed according to the Egyptian Standard Specifications (B.S Charts). The concrete used was cement (Sina Cement Company) (450 kg/m^3), natural siliceous sand, crushed dolomite coarse aggregate of maximum size 12.5 mm and super plasticizer's (Addicrete BVS type G) 1.8% from the weight of the cement. The mean strength was 40 MPa. The mix had a water-cement (w/c) ratio of 0.4, cement content of 450 kg/m^3, fine aggregate content of 628 kg/m^3, coarse aggregate content of 1144 kg/m^3, and super- plasticizer content of 8 kg/m^3.
Nine standard cubes with dimensions 150 mm x 150 mm x 150 mm were cast to perform concrete quality control. The cubes were immersed in water until the day of testing. The average 28-day strength achieved was the average compressive strength 40 MPa.

The yield strength and ultimate strength of smooth steel bars were 304 MPa and 415 MPa for 8 mm stirrups bars, 470 MPa and 636 MPa for 10 mm, and 566 MPa and 764 MPa for 12 mm, respectively. The results of steel bars are summarized in Tab. 2.

a) After installed shear connectors

b) Connection at the supports

Figure 2: Steel mesh and concrete of composite beam with external GFRP I-section.

No. of samples	Length (mm)	Diameter. (mm) Nominal	Actual	Tensile strength (Mpa) f_y	f_u	Elongation (%)	Specification Elongation
5	500	8	8.15	304	415	61	≥20%
5	500	10	10.12	470	636	32	≥16%
5	500	12	11.54	566	764	26	≥16%

Table 2: Results of Steel bars properties.

According to manufacturing date, the tensile strength of GFRP I-section was 336 MPa, and tensile modulus of elasticity 35300 MPa [23] as shown in Tab. 3.

No.	Item	Data
1	Specific gravity	1.85 g/cm^3
2	Tensile strength	336 MPa
3	Tensile modulus	35300 MPa
4	Flexural strength	334 MPa
5	Flexural modulus	73000 MPa
6	Compressive strength	327 MPa
7	Impact strength	2385 J/M
8	Hardness	52 HRC
9	Water-absorption rate	1.39 %
10	Heat distortion temperature	204℃

Table 3: GFRP I-section properties.

Test setup and instrumentation

The testing frame shown in the lower part of Fig. 3 was fixed to the strong solid floor of the RC laboratory of the Faculty of Engineering at Helwan University. The supporting structure consisted of a horizontal frame made of four steel I-beams. It was supported by four vertical steel I-beam legs fixed to the solid floor and the tested beams were supported on the frame. The loading was achieved by using a cell with a capacity of 1250 kN, which transferred the load to a high stiffness steel plate at two points in the middle of the beams; with a length of the pure bending area was 400 mm, setup as shown in the upper part of Fig. 3.

Figure 3: Four points loading that transfer from load cell to beams.

The load was measured using 1250 kN capacity load cell connected to a digital display unit with loading rate (5-10) kN. The load was applied in increments. An initial increment at low load was performed for every beam to verify that mechanical and electrical equipment was working properly. The deflections were measured at mid-span and quarter-span of beams at the points shown in Fig. 4a. The load had a control in deflection; the deflections were measured using two linear variable differential transducers (LVDTs) and one dial gauge (DGs) with 0.01 mm accuracy. The (LVDTs) and (DGs) were placed on the bottom surface of the beams. Three electrical strain gauges were used to measure the strain in GFRP I-section and steel bars at the maximum tensile point of GFRP I-section and steel bars. The strain gauges were affixed on the bottom longitudinal bars and the GFRP I-section top and bottom flanges as shown in Fig. 4b. This location was maintained for all tested beams.

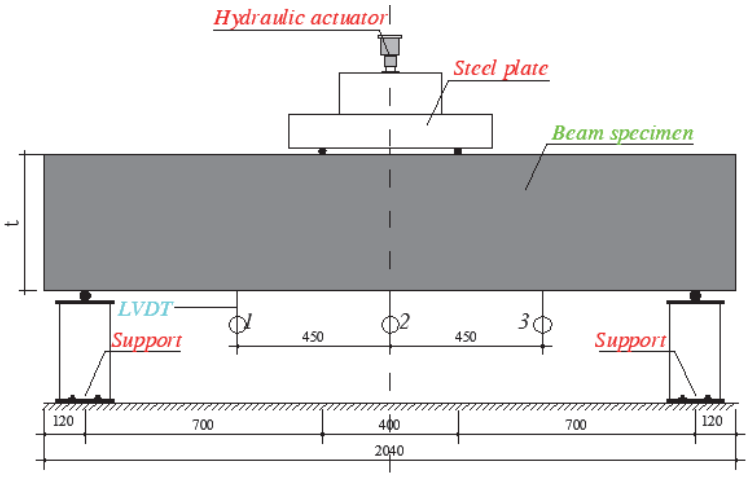

a) Deflection position

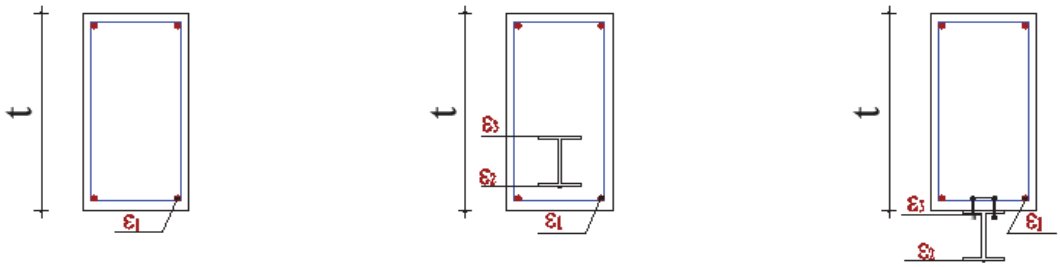

a) RC b) GFRP I-Internal c) GFRP I-External

b) Strain position

Figure 4: Test Setup: LVDT, DG and strain gauges of beams.

Fire testing procedures

The RC beam specimens were tested with fire after testing the control tested specimens of each. The control tested composite beam specimens RC1GI-I, RC2GI-I, and RC3GI-I have cracking load equal to 83.85 kN, 106.97 kN, and 130.09 kN respectively. In the first, the composite tested beams under fire RC1GI-I-F, RC2GI-I-F, and RC3GI-I-F tested without fire up to load equal to 91.47 kN, 130.60 kN, and 189.95 kN receptivity. The corresponding deflection curve had equal to 2.81 mm, 2.90 mm, and 2.22 mm respectively. The remaining deflection after removing the load is 0.58, 0.90 and 0.74 mm respectively. After exposing the tested specimens to fire as shown in Fig. 5 (500°C for 90 minutes), the beam is loaded to failure. A wired digital reader with thermal sensor was used to stabilize the temperature at 500 degrees for 90-minutes duration.

Figure 5: Specimens during the fire.

RESULTS AND DISCUSSION

Crack patterns and failure modes

Fig. 6 shows that all tested specimens that were exposed to flexural cracking occurred in the pure bending region and some prominent cracks were found within the two loading points. However, in terms of cracks number, it has been observed that the cracks in composite beams are similar to the cracks in traditional reinforced concrete beams. All the tested specimens were failed in flexure in addition to web shear in composite beams with external GFRP I-section, but this occurred after the beams had reached their yield load strength. The GFRP I-section ruptured with loud noises within the loading stages, but after the tensile steel bars reached their yield strength, and the specimen yielded, the top flanges and the bottom flanges could not reach the ultimate compressive or tensile strength for composite beams with an internal GFRP I-section, and the concrete on the compression side was crushed for some beams.

Beam cracking started gradually and continued during all the testing procedure with sound increased gradually until the load approached almost its maximum, then the main cracks became wider.

Load–deflection curves

As in Fig. 7, Deflection values are measured at the mid-span for composite beams. The load deflection relationships of the tested specimens show a linear part representing the un-cracked elastic stage, followed by a non–linear part which is divided into the cracking and yielding zones. First zone represents elastic behavior pre concrete cracking. In second zone, the cracked stage forms a part of the ascending branch of the curve with reduced stiffness. When the yield point is reached, the stiffness is greatly reduced and significant deflections occur. For the GFRP- composite concrete beams, the load deflection curves at mid-span of specimens had a same behavior as well. The curves firstly increased practically linearly until the yield load was reached. Then, the load dropped suddenly and increased many times up to the maximum load, which was followed by a continuous loud noise produced by the fracture of the GRP I-section and the composite beam specimens were stopped due to the slip that occurred between the I-section and the concrete. It is also possible that the shear stress in an external GFRP I-section web caused the failure, as was the case for specimens RC1GI-E, RC2GI-E, and RC3GI-E.

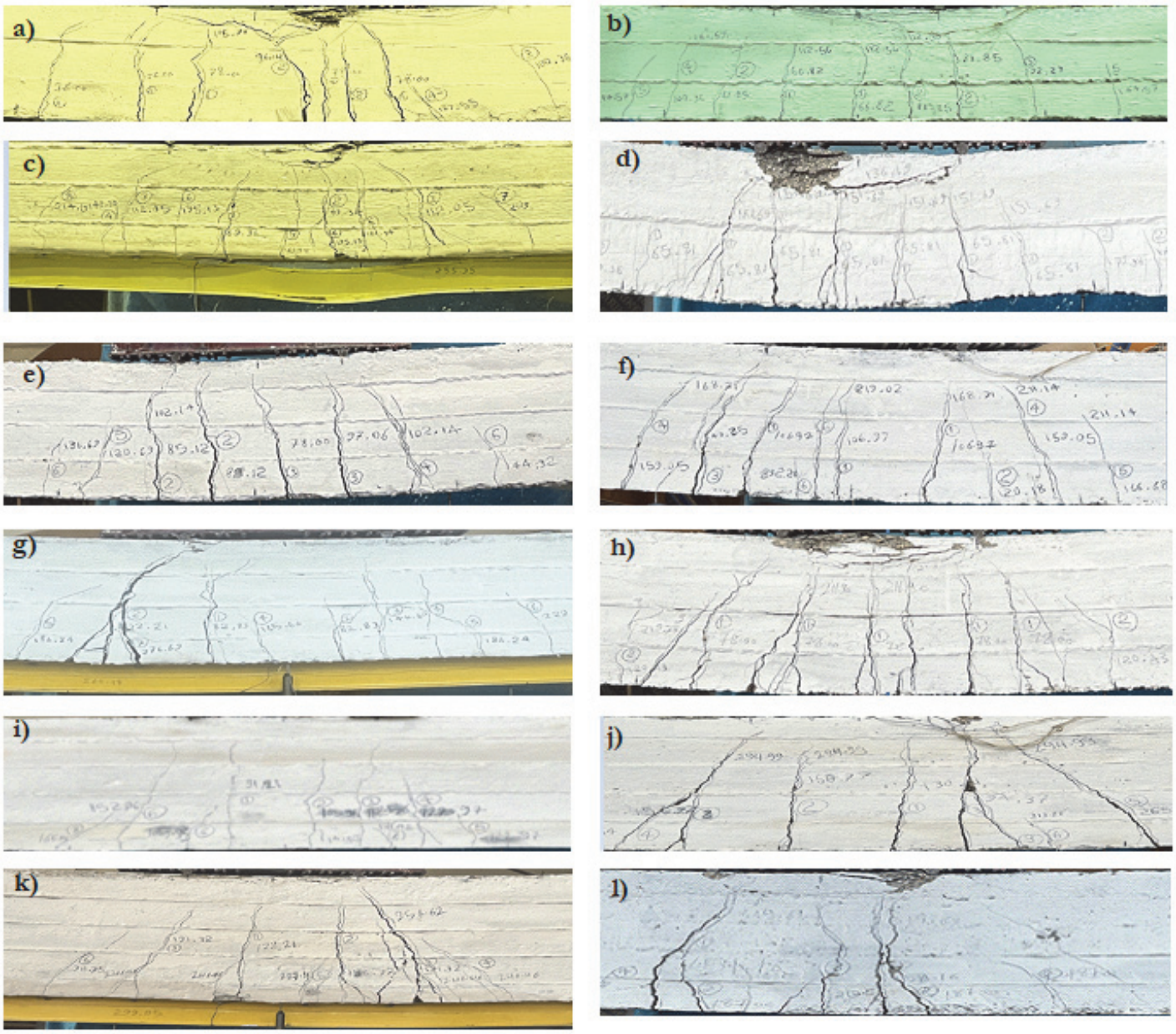

Figure 6: Failure modes of tested beams: a) RC1, b) RC1GI-I, c) RC1GI-E, d) RC1GI-I-F, e) RC2, f) RC2GI-I, g) RC2GI-E, h) RC2GI-I-F, i) RC3, j) RC3GI-I, k) RC3GI-E, l) RC3GI-I-F.

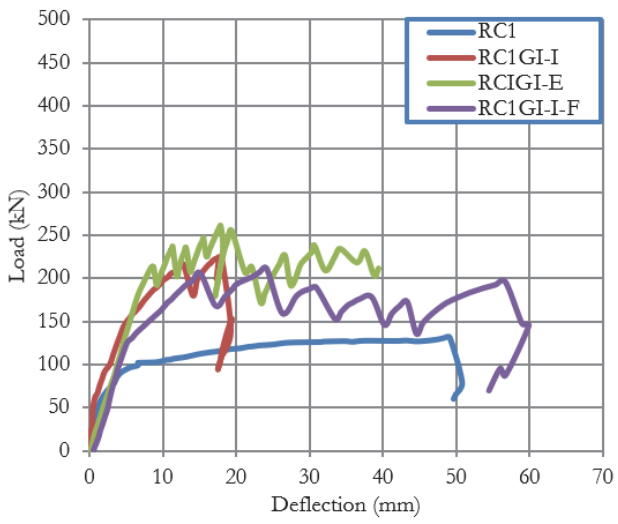

a) Beam height 300 mm

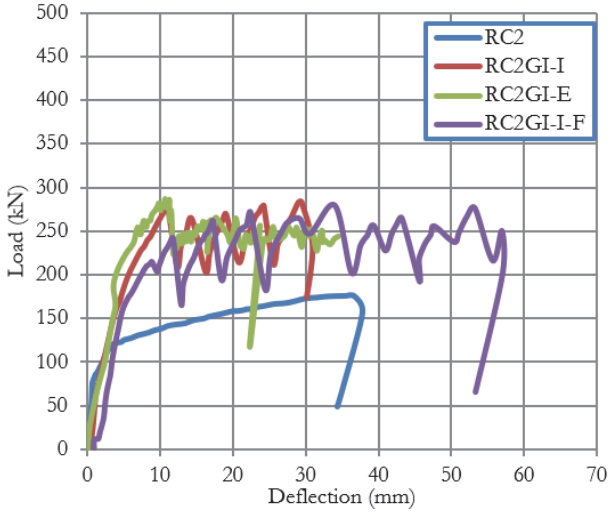

b) Beam height 400 mm

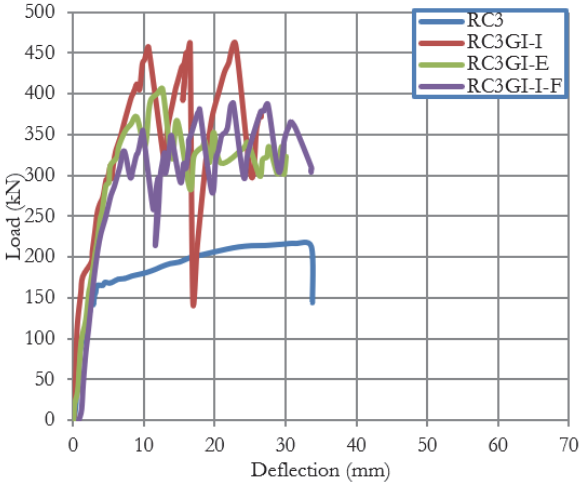

c) Beam height 500 mm

Figure 7: The load-deflection curves for beams.

The comparison between the conventional and the composite I-section reinforced beam shows that composite beams have much more strength and stiffness than conventional beams. However, the ultimate load of the beams exposed to fire is not significantly different from that of the composite beams without fire exposure.

Load strain curves

The measured load-strain curves for the composite and strengthened beams are shown in Fig. (8 & 9). During the pre-cracking stage, all the bottom reinforcement bars and the GFRP I-section recorded low strains. Once yielding had occurred, there was a sudden increase in the rate of strain development in the steel reinforcement bars and GFRP I-section. In general, the maximum strain in the steel bars reached more than the yielding strain. The strain measured in the bottom and top GFRP I-section, remained less than the yield strain in bottom steel bars, according to its location and distance from the neutral axis of the composite section.

The strain measured in the upper flange of GFRP I-section of strengthened beams decreased to half the value of the strain in the tensile steel as a result of sliding between the two surfaces, concrete and GFRP I-section, while it was equal to the value of the strain in the tensile steel bars in the lower flange.

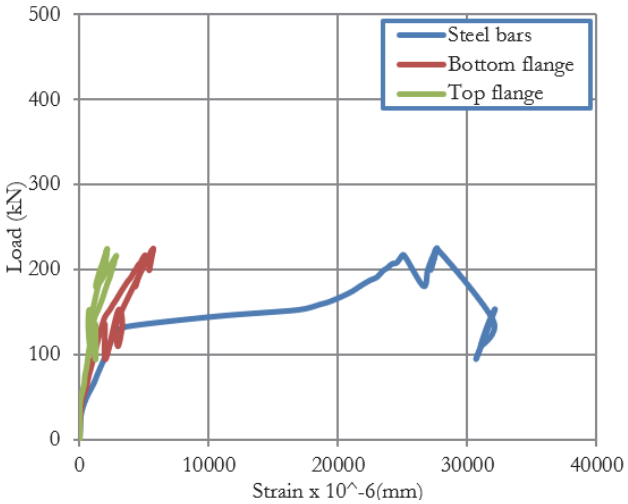

a) Beam height 300 mm

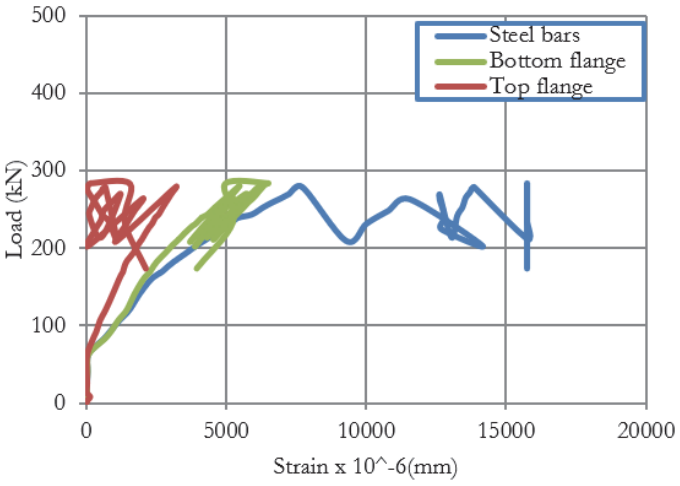

b) Beam height 400 mm

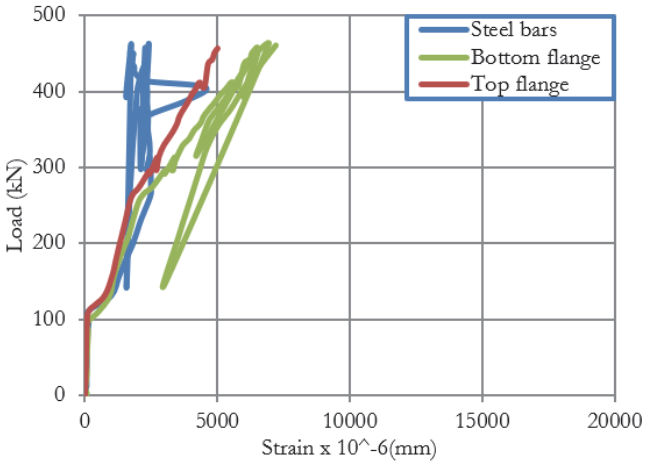

c) Beam height 500 mm

Figure 8: The load-strain curves for composite beams.

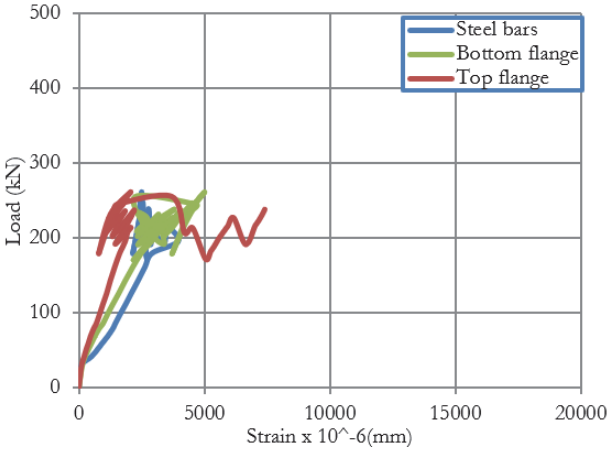

a) Beam height 300 mm

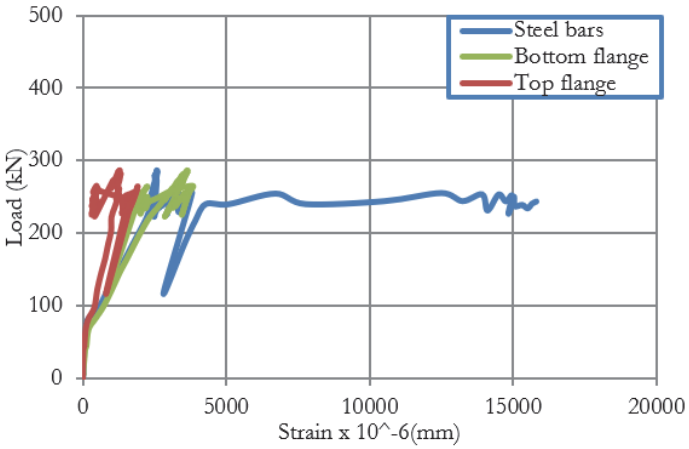

b) Beam height 400 mm

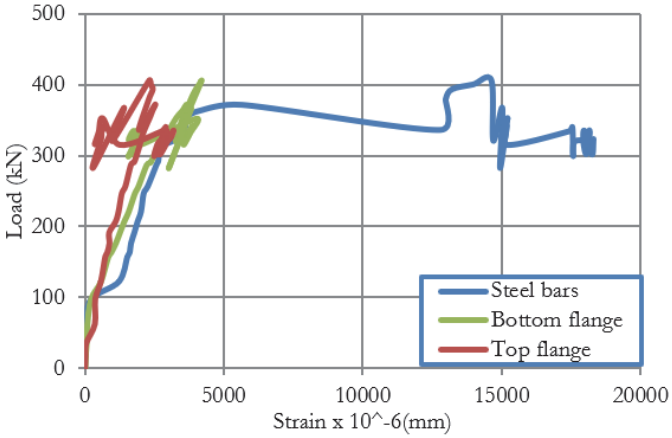

c) Beam height 500 mm

Figure 9: The load-strain curves for strengthened beams.

The ultimate load and the corresponding deflection

The ultimate loads and corresponding mid-span vertical deflections are summarized in Tab. 4. The results show that the composite reinforced beams with internal or external GFRP I-section achieved 162% to 213% of the capacity of the conventional R.C beams. The composite reinforced beams with internal GFRP I-section exposed to firing achieved 84% to 98% of the capacity of the composite R.C beams with internal GFRP I-section without firing.

In Fig. 9, the highest ultimate load value was for the composite reinforced concrete beams with internal GFRP I-section and the lowest ultimate load value was for the composite beam of 500 mm height exposed to fire.

Beam thickness (mm)	Specimens code	Ultimate load (kN)	Vertical deflection (mm)	$P_u/P_{u\ CTRL}$	δ/δ_{CTRL}
300	RC1	131.61	49.10	1.00	1.00
	RC1GI-I	224.86	17.60	1.71	0.36
	RC1GI-E	261.19	17.93	1.98	0.37
	RC1GI-I-F	212.16	24.17	0.94	1.37
400	RC2	175.82	35.22	1.00	1.00
	RC2GI-I	284.06	29.22	1.62	0.83
	RC2GI-E	287.36	10.68	1.63	0.30
	RC2GI-I-F	278.98	34.00	0.98	1.16
500	RC3	216.48	31.40	1.00	1.00
	RC3GI-I	461.92	16.47	2.13	0.52
	RC3GI-E	405.51	12.61	1.87	0.40
	RC3GI-I-F	388.23	22.65	0.84	1.38

Table 4: The experimental results.

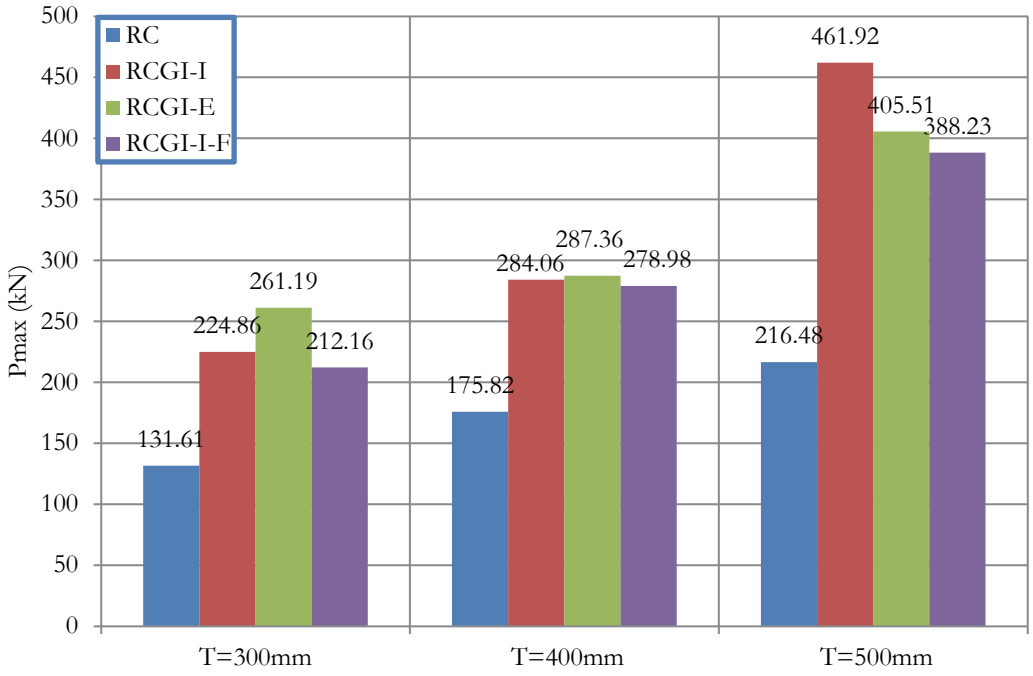

Figure 10: The ultimate load for all specimens compared with conventional beams

As shown in Tab. 4, for all groups, the maximum vertical deflection of the composite beams with GFRP I-section was smaller than that of the conventional beams. For 300 mm composite beams height, the deflection at the ultimate load decreased to 36% and 37% for internal and external GFRP I-section, respectively.

For 400 mm composite beams height, the deflection at the ultimate load decreases to 83% and 30% for internal and external GFRP I-section, respectively.

For 500 mm composite beams height, the deflection at the ultimate load decreased to 52% and 40% for internal and external GFRP I-section, respectively.

It can be concluded that, the composite beams with internal GFRP I-section cause larger deflections than the composite beams with external GFRP I-section. This is related to the increase in the depth of the composite external GFRP I-section beams.

Stiffness

Stiffness is an important parameter to measure the resistance of composite beams deformation under applied load. The initial stiffness is the slope of the load deflection curve from zero point to the cracking point. The non-linear behavior of composite beams measured approximated into two tangents after the cracking point .

For 300 mm beam depth, the stiffness of the internal and external composite specimens is 46.33 kN/mm and 25.31 kN/mm respectively, while the control specimen stiffness is 22.94 kN/mm.

For 400 mm beam depth, the stiffness of the internal and external composite specimens is 45.52 kN/mm and 46.27 kN/mm respectively, while the control specimen stiffness is 108.33 kN/mm.

For 500 mm beam depth, the stiffness of the internal and external composite specimens is 185.84 kN/mm and 69.83 kN/mm respectively, while the control specimen stiffness is 81.44 kN/mm.
The internal and external composite beams are significantly increased at the post-cracking stiffness. The stiffness of internal GRFP I-section beams with depths 300 mm, 400 mm, and 500 mm is 7.61, 2.32, and 5.09 respectively compared to conventional beam, while the stiffness of external GRFP I-section beams is 10.77, 8.11 and 6.31 respectively compared to conventional beams.
The fire has significant effect on the stiffness of internal GRFP I-section. The initial stiffness is 23.37 kN/mm, 26.35 kN/mm, and 52.94 kN/mm while the stiffness of GRFP I-section specimens without fire is 46.33 kN/m, 45.52 kN/mm, and 185.84 kN/mm for beams with depths equal to 300 mm, 400 mm, and 500 mm respectively. The post-cracking stiffness of specimens is decreased to 0.73, 0.98, and 0.64 compared to specimens without fire for beams with depths equal to 300 mm, 400 mm, and 500 mm respectively. Tab. 5 presents the stiffness of all tested specimens at all stages of loading and Fig. 11 compares the stiffness for all tested composite beams.

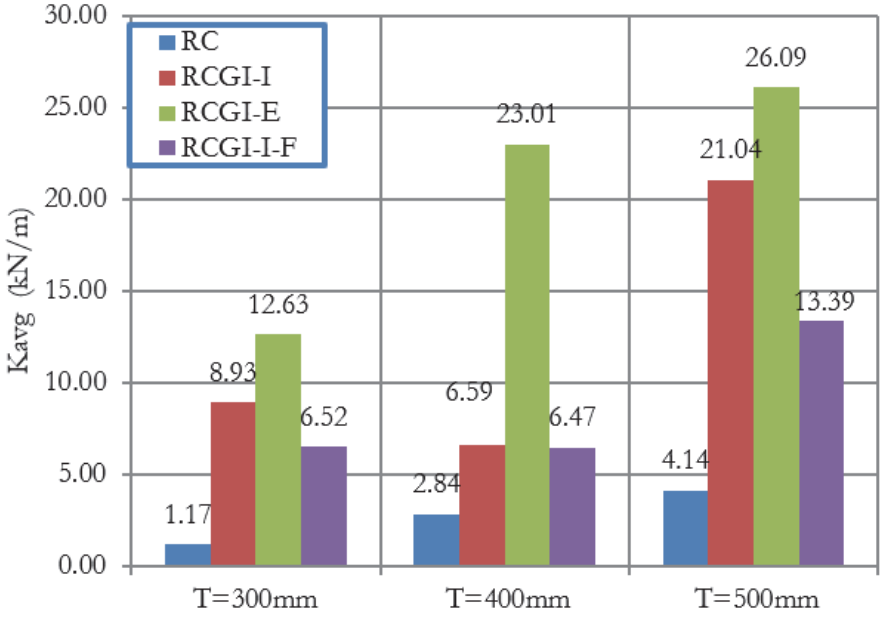

Figure 11: Average stiffness of tested specimens.

Beam thickness (mm)	Specimens code	$K_{initial}$ (kN/mm)	K1 (kN/mm)	K2 (kN/mm)	K_{avg} (kN/mm)	K_{avg}/ $K_{avgCTRL}$
300	RC1	22.94	8.85	0.81	1.17	1.00
	RC1GI-I	46.33	20.47	6.94	8.93	7.61
	RC1GI-E	25.31	28.27	7.21	12.63	10.77
	RC1GI-I-F	23.37	25.41	4.52	6.52	0.73
400	RC2	108.33	15.47	1.78	2.84	1.00
	RC2GI-I	45.52	30.21	4.26	6.59	2.32
	RC2GI-E	46.27	34.00	9.99	23.01	8.11
	RC2GI-I-F	26.35	37.06	3.76	6.48	0.98
500	RC3	81.44	31.92	2.14	4.14	1.00
	RC3GI-I	185.84	41.52	15.27	21.04	5.09
	RC3GI-E	69.83	54.47	12.70	26.09	6.31
	RC3GI-I-F	52.94	53.06	7.03	13.39	0.64

Table 5: Stiffness for tested specimens.

Ductility index

The ductility index (μ_δ) of all tested composite beams is calculated as the ratio between the maximum deflection at the ultimate load and the deflection at the yield point ($\mu_\delta = \delta_u/\delta_y$) [24] as listed in Tab. 6. The yield point is the point where the beam stiffness decreases to the ultimate point as shown in Fig. 12. The traditional reinforced concrete beam exhibited the largest ductility of all the groups followed by the composite beam with internal GRFP I-section exposed to fire then the composite beam with internal GRFP I-section without fire and then the least ductility was achieved by the composite beam with external GRFP I-section. The ductility decrease in the composite beams due to the reduction in beam deflection at the same load levels compared to the traditional reinforced concrete beam by comparing the calculated ductility ratio of all tested specimens.

Beam thickness (mm)	Specimen code	Yield point (δ_y) (mm)	Ultimate point (δ_u) (mm)	Ductility index (μ_δ)	$\mu_\delta/\mu_{\delta CTR.}$
300	RC1	5.76	49.10	8.99	1.00
	RC1GI-I	4.44	17.60	4.26	0.47
	RC1GI-E	6.65	17.93	2.70	0.30
	RC1GI-I-F	5.87	24.17	4.61	1.08
400	RC2	3.28	35.22	10.45	1.00
	RC2GI-I	6.07	29.22	6.14	0.59
	RC2GI-E	6.61	10.68	1.62	0.15
	RC2GI-I-F	7.68	34.00	6.19	1.01
500	RC3	3.25	31.40	9.97	1.00
	RC3GI-I	4.63	16.47	3.95	0.40
	RC3GI-E	5.23	12.61	2.41	0.24
	RC3GI-I-F	5.75	22.65	4.55	1.15

Table 6: Ductility index (μ_δ) of tested specimens.

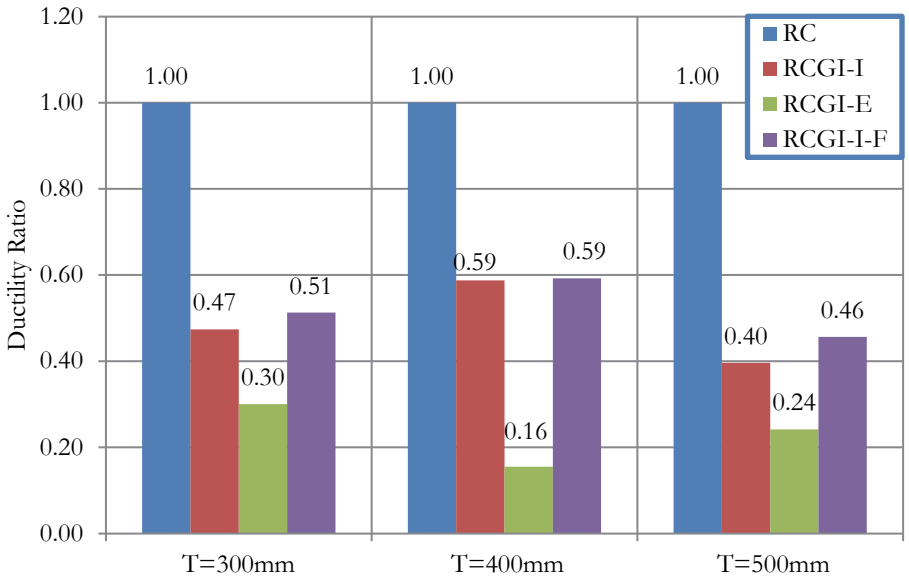

Figure 12: Ductility ratio for specimens.

Ductility of energy

The ductility of energy (μ_E), as shown in equation is based on the energy theory which was proposed by Naaman et al. [25]. This equation could be used to calculate the ductility without identifying the yield point of the specimen.

$$\mu_E = \frac{1}{2}\left(\frac{E_T}{E_E} + 1\right) \tag{1}$$

where E_T is the total energy calculated by the area under the load mid-span deflection curve.

E_E is the elastic energy (Fig. 13), which is calculated by the area under the slope of the elastic behavior.

Traditionally, the weighted value of S_1 and S_2 is used to obtain the slope of the elastic zone region (S) in Eqn. 2 below.

$$S = \frac{P_1 S_1 + (P_2 - P_1) S_2}{P_2} \tag{2}$$

where S_1 and S_2 are the slopes of the initial two lines on the load mid-span deflection curve

P_1 and P_2 are the loads at the end of the two lines, respectively.

Tab. 7 shows the energy ductility of the beam specimens. In terms of ductility energy area ratio, 0–69% represents brittleness, 70%–74% represents semi-ductility, and 75%–100% represents ductility [26]. All specimens are more ductile (86 to 95%), but only 81% for RC1GI-I specimen only.

Beam thickness (mm)	Specimen code	Load (kN)		Slope			Energy				Energy ductility
		P_y	P_u	S1	S2	S	Total E_T	Elastic E_E	Inelastic	Rate	
300	RC1	96.24	131.61	39.43	1.68	29.29	5796	296	5500	0.95	10.30
	RC1GI-I	131.34	224.86	62.14	9.73	40.34	3231	627	2604	0.81	3.08
	RC1GI-E	179.89	261.19	27.07	22.04	25.50	7741	1053	6689	0.86	4.18
	RC1GI-I-F	126.53	212.16	33.33	8.62	23.36	9847	826	9021	0.92	6.46
400	RC2	119.00	175.82	93.01	2.80	63.86	5631	192	5439	0.97	15.18
	RC2GI-I	179.77	284.06	55.86	14.43	40.65	6855	987	5868	0.86	3.97
	RC2GI-E	246.71	287.36	49.17	14.56	44.27	7922	675	7247	0.91	6.37
	RC2GI-I-F	171.76	278.98	39.51	8.74	27.68	12579	1127	11453	0.91	6.08
500	RC3	156.00	216.48	89.85	2.68	65.49	6359	344	6015	0.95	9.73
	RC3GI-I	274.15	461.92	185.31	60.03	134.38	9054	529	8526	0.94	9.06
	RC3GI-E	311.76	405.51	86.34	27.25	72.68	9277	770	8507	0.92	6.52
	RC3GI-I-F	263.99	388.23	82.24	22.70	63.19	10176	1058	9118	0.90	5.31

Table 7: Ductility of energy (μE) of tested specimens.

Fig. 13 shows that the traditional reinforced concrete beams in all groups had higher ductility than the other beam specimens.

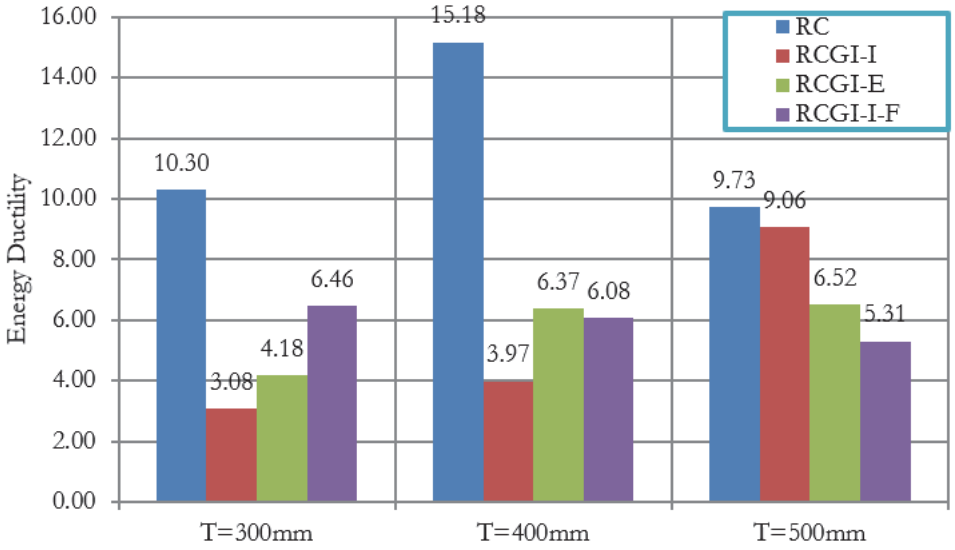

Figure 13: Comparison of energy ductility of tested specimens.

THEORETICAL ANALYSIS

The ability of common structural analysis tools to predict the performance of the tested composite beams was investigated in order to provide practicing engineers with information about their respective reliability. Both the Linear analysis method and the first principle method were considered.

The first principle method was used in this study to analyze the tested composite beams and calculate the maximum bending moment to ensure that the beams flexural strength meets or exceeds design standards.

Strain compatibility of composite beams refers to ability of various materials, as concrete, steel and GFRP, to work together harmoniously under different loads and conditions. The key aspect of strain compatibility is to ensure that all both materials within the beam experience similar strains and deformations when subjected to external forces. By achieving strain compatibility, composite beams can effectively distribute stress between the materials, preventing premature failure or excessive deflection**.**

Determine the strain level in the GFRP at the ultimate (yield) limit state. Because GFRP materials are linear elastic until failure, the level of strain in the GFRP will dictate the level of stress developed in the GFRP. The maximum strain level that can be achieved in the GFRP is determined by either the strain level developed in the GFRP at the point at which the concrete crushes, or the point at which the GFRP ruptures.

Nominal moment strength of steel reinforced only

The first principles procedure involves calculating the distance from the neutral axis to the end of compressed concrete by producing the corresponding stress level and confirming the equilibrium of internal force. In case of non-equilibrium, the neutral axis depth should be updated and the steps are repeated.

The resisting moments are obtained from Eqn. 3 according to Egyptian code of practice (ECP-203) [27].

$$M_n = \left(A_s - A_s^{'}\right) f_y \left(d - \frac{a}{2}\right) + A_s^{'} \; f_s^{'} \left(d - d'\right) \tag{3}$$

Nominal moment strength of internal GFRP composite beams

The internal strain and stress distribution for the composite beam specimen under flexure at the ultimate limit state is shown in Fig. 14.

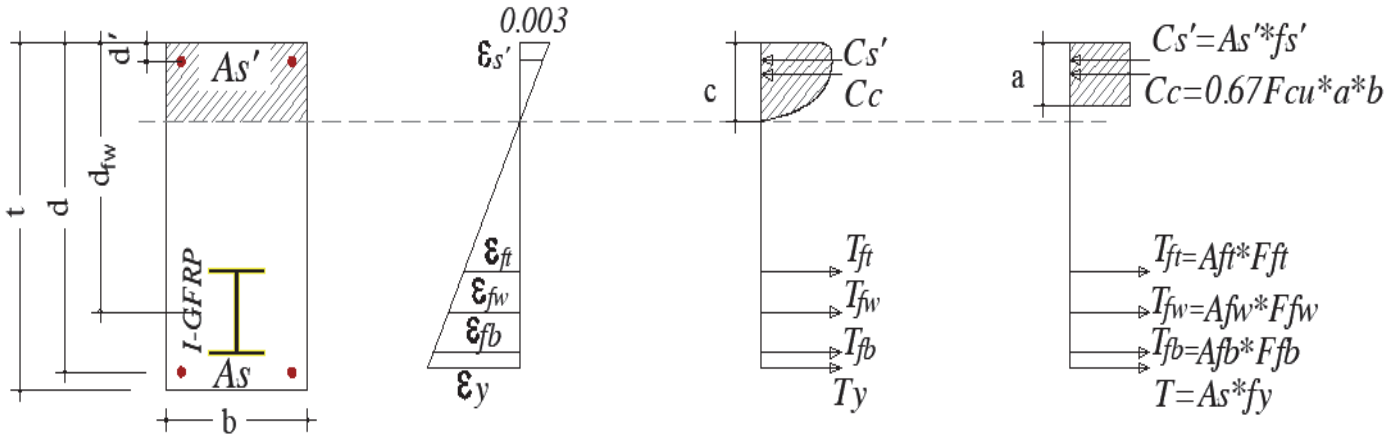

RC section Strain Nonlinear stress Equivalent stress

Figure 14: Internal strain and stress distribution of composite sec. at ultimate limit state.

Resisting moments for composite beams with steel I-sections can be found according to AISC 360 [28] and Eurocode 4 [29] from the theoretical Eqn. 4.

$$M_n = \left(A_s - A_s^{'}\right) f_y \left(d - \frac{a}{2}\right) + A_s f_y \left(d - \frac{a}{2}\right) + A_s^{'} \; f_s^{'} \left(d - d'\right) \tag{4}$$

Therefore, the resisting moments for GFRP I-sections can be calculated by modifying the previse Eqn. 4 to proposed theoretical Eqn. 5.

$$M_n = \left(A_s - A_s^{'}\right) f_y \left(d - \frac{a}{2}\right) + A_s f_{fe} \left(d_f - \frac{a}{2}\right) + A_s^{'} \; f_s^{'} \left(d - d'\right) \tag{5}$$

$$f_{fe} = \varepsilon_f E_f \tag{6}$$

$$\varepsilon_f = \frac{d_f - c}{c} 0.003 \le \varepsilon_f allowable \tag{7}$$

where:

A_f The area of the GFRP I-section
d_f The distance from the extreme compression concrete fiber to the center of the GFRP
E_f Tensile modulus of elasticity of GFRP
f_{fe} Effective stress in the GFRP I-section; stress level attained at section failure
k_f Sliding coefficient between an external GFRP I-section and concrete equal to 0.75
ε_f The strain in the GFRP

Nominal moment strength of beam section strengthened with external GFRP I-section

The friction coefficient (k_f) represents the resistance of sliding along surfaces between concrete and external GFRP. Accurate estimation of this slip is essential for predicting the behavior of composite beams under various loading conditions and designing reliable connections between GFRP members and concrete components. The strain in the upper flange decreases to half the strain value in the tensile steel, while it is equal to the strain value in the tensile steel in the lower flange as shown in Fig. 15. We can quantify the friction coefficient k_f to ensure safe and efficient designs that optimize the performance of GFRP based-beams through experimental tests, which is equal to 0.75 in this experiment. The internal strain and stress distribution for a rectangular section reinforced with steel bars and externally strengthened with GFRP I-section under flexure at the ultimate limit state are shown in Fig. 15.

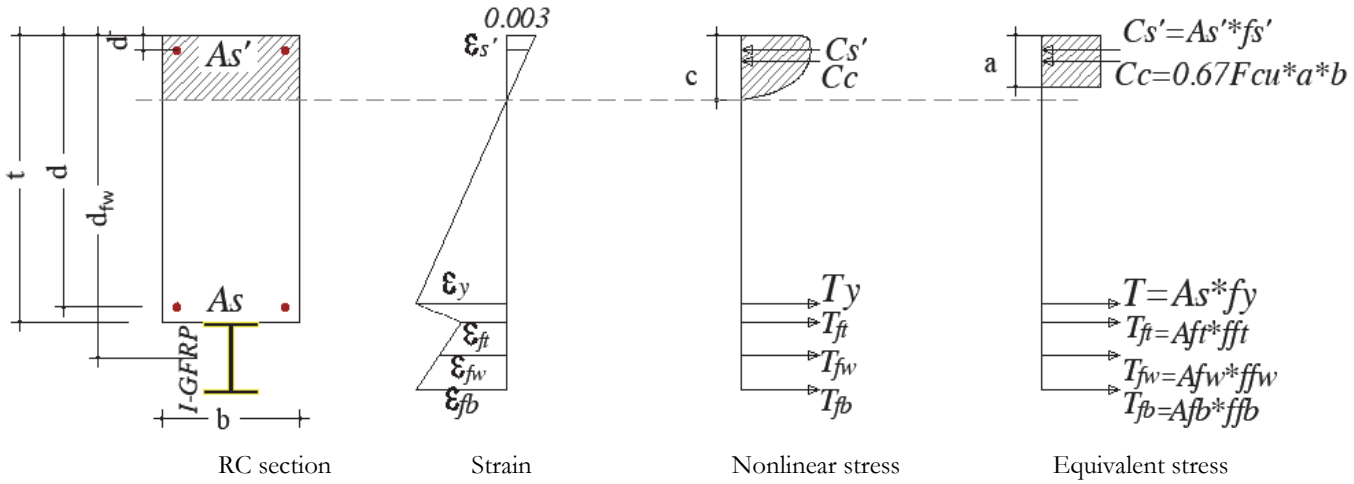

Figure 15: Internal strain and stress distribution of strengthened sec. at ultimate limit state.

Resisting moments can be found from proposed theoretical Eqn. 5.

$$M_n = \left(A_s - A_s^{'}\right) f_y \left(d - \frac{a}{2}\right) + A_s f_{fe} \left(d_f - \frac{a}{2}\right) + A_s^{'} \; f_s^{'} \left(d - d'\right) \tag{8}$$

$$f_{fe} = k_f \varepsilon_f E_f \tag{9}$$

However, in the experimental study, the nominal moment strength is calculated with the use of strain compatibility method for the different elements at the moment when the strain in the reinforcement is equal to the yield strain, therefore the nominal moments are calculated as shown in the previous equations but by replacing the term (a/2) with (z/3) and the concrete compressive stress ($0.67F_{cu}ab$) with ($\varepsilon_c E_c zb/2$) according to Fig. 16.

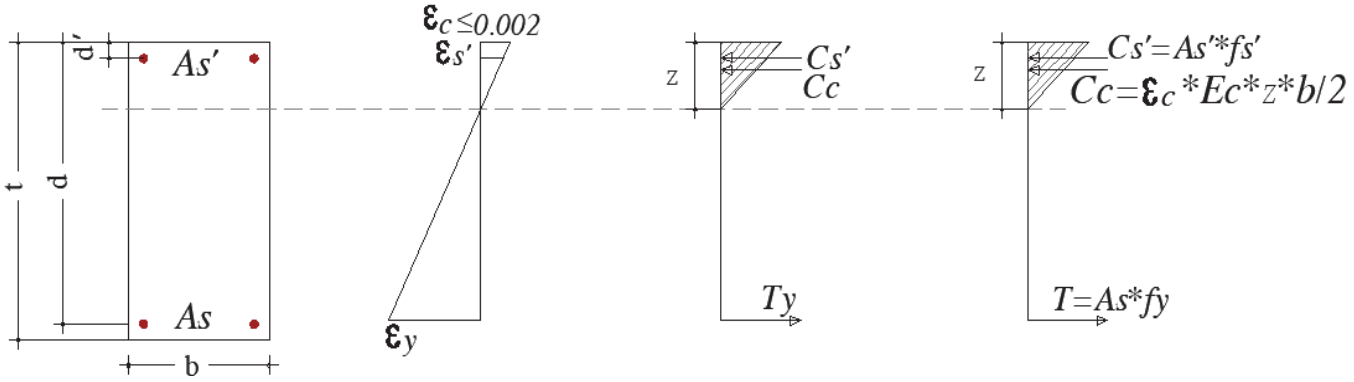

Figure 16: Internal strain and stress distribution at main steel yield strain.

By comparing the experimental strain readings with the analytical values of the traditional RC and composite beams, the strains is very closely at the yield moment as shown in Tab. 8**.** In the external case, it was found that the experimental strain is more than theoretical due to the separation between the GFRP I-section and concrete.

Type	Specimen code	Exp. Strain x 10^-6 (mm)			Analy. Strain x 10^-6 (mm)			$\varepsilon_{Exp.}$ / $\varepsilon_{Analy.}$			
		Steel	Bottom flange	Top flange	Steel	Bottom flange	Top flange	Steel	Bottom flange	Top flange	Avg. GFRP
Conventional Beams	RC1	2830	-------	-------	2830	-------	-------	1.00	-------	-------	-------
	RC2	2830	-------	-------	2830	-------	-------	1.00	-------	-------	-------
	RC3	2830	-------	-------	2830	-------	-------	1.00	-------	-------	-------
Internal Composite Beams	RC1GI-I	2830	1677	989	2830	2426	1080	1.00	0.69	0.92	0.80
	RC2GI-I	2830	2463	1399	2830	2352	1394	1.00	1.05	1.00	1.03
	RC3GI-I	2830	2552	2042	2830	2607	1862	1.00	0.98	1.10	1.04
External Composite Beams	RC1GI-E	2830	2486	1630	2830	2830	1415	1.00	0.88	1.15	1.02
	RC2GI-E	2830	2832	1189	2830	2830	1415	1.00	1.00	0.84	0.92
	RC3GI-E	2830	2629	1965	2830	2830	1415	1.00	0.93	1.39	1.16

Table 8: Comparison between experimental strains reading with the analytical values.

By comparing between the experimental results and the proposed theoretical equation of the composite section, the results is very closely to the yield moment, which indicating the reliability of the results that no significant differences in the yield moments were found as shown in Fig. 17 and Tab. 9**.**

The theoretical calculations and the precision of the proposed design were able to accurately predict the flexural behavior of composite and strengthened beams taking into consideration the value of the interface slip between GFRP profile and the concrete.

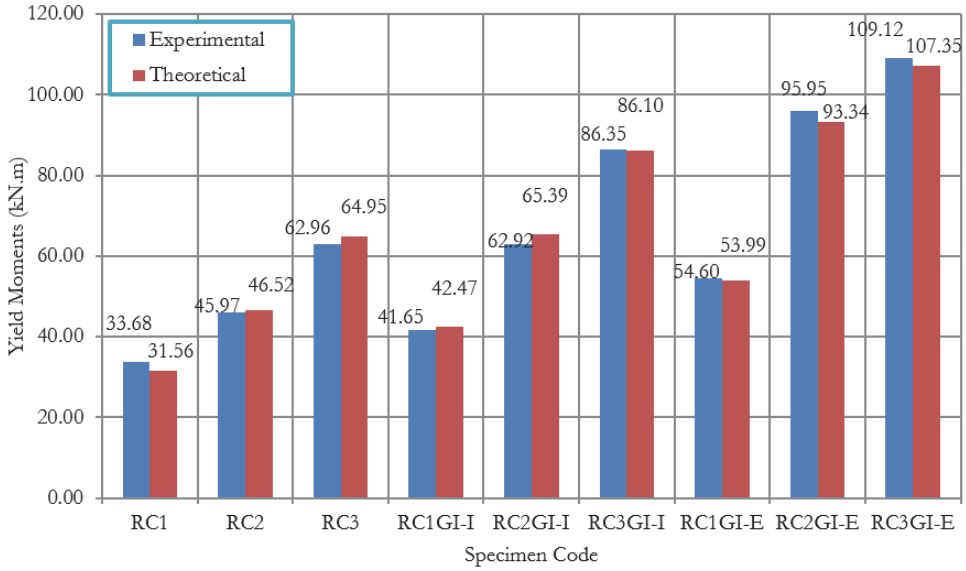

Figure 17: Comparison between experimental and theoretical yield moments.

Type	Specimen code	Yield moments (M_y) (kN.m)		$M_{exp.}$ / $M_{theo.}$
		$M_{exp.}$	$M_{theo.}$	
Conventional Beams	RC1	33.68	31.56	1.07
	RC2	45.97	46.52	0.99
	RC3	62.96	64.95	0.97
Internal Composite Beams	RC1GI-I	41.65	42.47	0.98
	RC2GI-I	62.92	65.39	0.96
	RC3GI-I	86.35	86.10	1.00
External Composite Beams	RC1GI-E	54.60	53.99	1.01
	RC2GI-E	95.95	93.34	1.03
	RC3GI-E	109.12	107.35	1.02

Table 9: Comparison between experimental and theoretical results of beams.

CONCLUSIONS

From experimental and theoretical results on the flexural behavior of the proposed composite beams reinforced with steel bars and (GFRP) I-section, the following conclusions can be drawn**:**

- Glass Fiber Reinforced Polymer (GFRP) I-section composite concrete beams proved to be an efficient

structure element with a high bending capacity and bending stiffness. However, the energy ductility was lower as the elastic modulus of GFRP profile .

- Compared with the conventional reinforced concrete beam, the composite beam with internal GFRP I-section showed 62% to 113% higher ultimate capacity and 63% to 98 % with external GFRP I-section, and less deflection at the same level.
- The behavior of composite beams reinforced with steel bars and GFRP I-section exposed to fire at 500°C for one and half hours exhibited a very small effect for fire exposure, not exceeding 5% for the yield load.
- Compared with the beams strengthened with the external I-section, the fire performance of the composite beams is increased because the I-section is protected by the surrounding concrete, the stability of the I-section is increased because of the concrete casing, and then, the bond between the concrete and I-section can be increased.
- GFRP profile is more efficiently utilized when placed near close to the tensioned fiber and the bottom flange of the I-section is highly utilized and is more efficient than the top flange. In addition, the bottom flange can provide high tensile strength .
- Slip occurs between the concrete and the GFRP profile, which reduces the load-carrying of the beam specimens to some extent but only after the yield strength is reached .
- For beams exposed to negative bending moments, the bottom flange of the external GFRP I-section under compression causes mostly lateral torsional buckling, with confirmation to prevent the top flange local buckling, so it is no longer fully attached by the concrete beam.
- For beams strengthened externally with GFRP I-section, the strain in the upper flange decreases to half the value of the strain in the tensile steel, while it is equal to the value of the strain in the tensile steel in the lower flange and the sliding occurs between the concrete and the GFRP profile.
- The crush failure of some of the GFRP I-section specimens refers that stiffeners should be placed under concentrated load areas to prevent early failure due to by high shear stress concentrations.

REFERENCES

[1] Ibrahim, T., Allawi, A. and El-Zohairy, A. (2022). Experimental and FE analysis of composite RC beams with encased pultruded GFRP I-beam under static loads, Advances in Structural Engineering, 26 (3), pp. 516-532, DOI: 10.1177/13694332221130795.

[2] Zhang, P., Zhang, Y., Yang, S., Liu, Y. and Ahmed, S. (2023). Experimental tests of FRP-HSC hybrid beams under four-point bending, Vol. 26 (10), pp. 1895-1910, DOI: 10.1177/13694332231157928.

[3] Ali, M., Allawi, A. and El-Zohairy, A. (2024). Flexural Behavior of Pultruded GFRP–Concrete Composite Beams Strengthened with GFRP Stiffeners, fibers, 12 (1), DOI: 10.3390/fib12010007.

[4] Enas, M., Ibrahim, T., Allawi, A. and El-Zohairy, A. (2023). Experimental and Numerical Behavior of Encased Pultruded GFRP Beams under Elevated and Ambient Temperatures, fibers, 6(5), DOI: 10.3390/fire6050212.

[5] Jian, S. and Muhammad, N. (2017). Flexural behavior of composite beams reinforced with GFRP I-section, 6th Asia-Pacific Conference on FRP in Structures, Singapore.

[6] Abbas, A. and Safaa, I. (2020). Flexural behavior of composite GFRP pultruded I-section beams under static and impact loading, Civil Engineering Journal, 6(11), pp. 2143-2158. DOI: 10.28991/cej-2020-03091608.

[7] Ibrahim, A. (2018). Long-time behavior of GFRP/concrete hybrid structures, 9th International Conference on Fiber-Reinforced Polymer (FRP) Composites in Civil Engineering, Paris.

[8] Muttashar, M. and Manalo, A. (2017). Flexural Behavior of Multi-Celled GFRP Composite Beams with Concrete Infill: Experiment and theoretical analysis, Composite Structures 159, pp. 21-33. DOI: 10.1016/j.compstruct.2016.09.049.

[9] Correia, J. R., Branco, F. A., Ferreira, J. G. (2009). Flexural behavior of multi-span GFRP-concrete hybrid beams, Engineering Structures 31 (7), pp.1369-1381. DOI: 10.1016/j.engstruct.2009.02.004.

[10] Correia, J. R., Branco, F. A., Ferreira, J. G. (2007). Flexural behavior of GFRP–concrete hybrid beams with interconnection slip, Composite Structure 77 (1), pp. 66-78. DOI: 10.1016/j.compstruct.2005.06.003.

[11] Pinto, R. and Vieira, D., Rovere, H. (2012). Structural behavior of composite concrete/GFRP beams, European conference on composite materials, Venice, Italy.

[12] Correia, J. R., Branco, F. A., Ferreira, J. G. (2009). GFRP–concrete hybrid cross-sections for floors of buildings, Engineering Structures 31 (6), pp. 1331-1343, DOI: 10.1016/j.engstruct.2008.04.021.

[13] Nordin, H. and Taljsten, B. (2004). Testing of hybrid FRP composite beams in bending, Composites Part B: Engineering 35(1), pp. 27-33, DOI: 10.1016/j.compositesb.2003.08.010.

[14] El-Hacha, R. and Chen, D. (2012). Behavior of hybrid FRP–UHPC beams subjected to static flexural loading, Composites Part B: Engineering 43(2), pp. 582-593, DOI: 10.1016/j.compositesb.2011.07.004.

[15] Shahaji, P. (2019). Experimental study on load carrying capacity of RCC beam by using pultruded Frp I- section & C-section, International Journal of Science and Research 8 (7), pp. 1128-1133, DOI: 10.21275/ART20199762.
[16] Kwan, W. and Ramli, M. (2013). Indicative performance of fiber reinforced polymer (FRP) encased beam in flexure, Construction and Building Materials 48, pp. 780-788, DOI: 10.1016/j.conbuildmat.2013.07.013.
[17] Keller, T. (2001). Recent all-composite and hybrid fiber-reinforced polymer bridges and buildings, Structural Engineering and Materials 3(2), pp. 132-140, DOI: 10.1002/pse.66.
[18] Eskenati, A., Mahboob, A., Bernat-Maso, E., and Gil, L. (2022). Experimental and numerical study of adhesively and bolted connections of pultruded GFRP I-shape profiles, Polymers 14 (5), DOI: 10.3390/polym14050894.
[19] Correia, M. (2012). Structural behavior of GFRP profiles experimental study and numerical modeling, higher technical institute, Engineering, Materials Science.
[20] Wang, L., Fan, X., Chen, H. and Liu, W. (2016). Axial crush behavior and energy absorption capability of foam-filled GFRP tubes under elevated and high temperatures, Composite Structure 149, pp. 339-350, DOI: 10.1016/j.compstruct.2016.04.028.
[21] Wong, P., Davies, M. and Wang, Y. (2004). An experimental and numerical study of the behavior of glass fiber reinforced plastics (GRP) short columns at elevated temperatures, Composite Structure 63 (1), pp. 33-43, DOI: 10.1016/S0263-8223(03)00122-3
[22] Aydin, F. (2016). Effects of various temperatures on the mechanical strength of GFRP box profiles, Construction and Building Materials 127, pp. 843-849 2016. DOI: 10.1016/j.conbuildmat.2016.09.130.
[23] OPCT, Fiberglass Products Company, 398 Kaiyuan Road, Jizhou District, Hengshui City, Hebei Province, China, www.Chopct.com.
[24] Apeh, J. and Okoli, O. (2016). Evaluation of ductility index of concrete beams reinforced with rebars milled from scrap metals, Concrete research, 7(2), DOI: 10.20528/cjcrl.
[25] Naaman, E. and Jeong, S. (1995). Structural ductility of concrete beams prestressed with FRP tendons, Proceedings of the second international RILEM symposium (FRPRCS-2): non-metallic (FRP) for concrete structures. Ghent, Belgium, pp. 379-386.
[26] Kim, T. and Park, J. (2021). Evaluation of the performance and ductility index of concrete structures using advanced composite material strengthening methods, Polymers, 13, DOI: 10.3390/polym13234239.
[27] Egyptian code for design and construction of reinforced concrete structures. (2018). ECPCS-203., Housing and Building National Research Center. Ministry of Housing, Utilities and Urban Planning, Giza, Egypt.
[28] Specification for structural Steel buildings (2010). (AISC 360). ANSI/AISC 360-10. Chicago (IL): American Institute of Steel Construction.
[29] Design of composite steel and concrete structures - Part 1-1: General rules and rules for buildings, (2004). EN 1994-1-1, Eurocode 4. London: British Standards Institution.